

## Solar wind implantation supplied light volatiles during the first stage of Earth accretion

S. Péron<sup>1\*</sup>, M. Moreira<sup>1</sup>, B. Putlitz<sup>2</sup>, M.D. Kurz<sup>3</sup>



### Abstract

doi: 10.7185/geochemlet.1718

The isotopic and elemental compositions of noble gases constitute a powerful tool to study volatile origin and evolution, due to their inertness, and can thus provide crucial information about the early stage of planetary formation. Two models are proposed to explain the light noble gas origin on Earth: the solar wind implantation model and the solar nebula gas dissolution model. However, noble gas measurements often show addition of air to the mantle-derived gas, which complicates the determination of mantle isotopic ratios. We analysed the noble gas isotopic compositions of single vesicles in samples from the Galápagos hotspot with laser ablation, in order to understand and remove this atmospheric component, as well as discriminate between the two scenarios. Based on the new high precision results and a new statistical approach, we show that the solar wind implantation model is more likely to explain the terrestrial He, Ne and Ar composition. This scenario could bring important constraints on the solar system environment during the early stage of planetary formation.

Received 12 October 2016 | Accepted 8 February 2017 | Published 13 March 2017

### Introduction

The isotopes  $^{20}\text{Ne}$ ,  $^{22}\text{Ne}$ ,  $^{36}\text{Ar}$  and  $^{38}\text{Ar}$  are primordial in the Earth's mantle, the  $^{20}\text{Ne}/^{22}\text{Ne}$  and  $^{38}\text{Ar}/^{36}\text{Ar}$  isotopic ratios can thus be used as noble gas source tracers. The major noble gas carriers in the solar system are, among others, the solar wind ( $^{20}\text{Ne}/^{22}\text{Ne} = 13.8\text{--}14.0$ ,  $^{38}\text{Ar}/^{36}\text{Ar} = 0.1818\text{--}0.1828$ ; Heber *et al.*, 2009; Pepin *et al.*, 2012), the component B ( $^{20}\text{Ne}/^{22}\text{Ne} = 12.5\text{--}12.7$ ,  $^{38}\text{Ar}/^{36}\text{Ar} = 0.1862$  or 0.1919; Black, 1972; Raquin and Moreira, 2009; Moreira, 2013; Moreira and

Charnoz, 2016), which corresponds to solar wind implantation and is mostly important for light noble gases, and the phase Q for heavy noble gases found in chondrites ( $^{20}\text{Ne}/^{22}\text{Ne} = 10.1\text{--}10.7$ ,  $^{38}\text{Ar}/^{36}\text{Ar} = 0.1873$ ; Busemann *et al.*, 2000). The lower mantle is one plausible reservoir of primitive noble gases (Allègre *et al.*, 1983), so some Oceanic Island Basalts (OIBs), which are presumed to sample the lower mantle, are of particular interest to determine the Earth's primordial isotopic ratios. Only a limited suite of samples from a few hotspots (Hawaii, Galápagos and Iceland) are suitable because unradiogenic/primitive (He, Ne) isotopic compositions are rare, and because submarine or subglacial glass samples are needed to analyse the primitive noble gas compositions. Such glass samples correspond to magma quenched at high pressures during eruptions and are among the best samples to record the mantle noble gas composition.

However, the ubiquity of an atmospheric component has complicated the determination of mantle source noble gas isotopic compositions. The air component may be derived from post-eruption contamination when samples are recovered from the seafloor (Ballentine and Barfod, 2000). It may also come from atmospheric recycling through subduction for heavy noble gases (Ar, Kr, Xe) (Holland and Ballentine, 2006; Kendrick *et al.*, 2011; Parai and Mukhopadhyay, 2015). Noble gas studies often use step-crushing to analyse samples, and the results yield mixing trends between an atmospheric end-member and a mantle end-member. It is then assumed that the highest measured value is the least air contaminated and corresponds to a lower limit for the mantle. However, this approach does not necessarily completely eliminate atmospheric contamination. In order to avoid the atmospheric component, laser ablation analyses were introduced (Burnard *et al.*, 1997; Burnard, 1999), which involve targeting individual bubbles with a laser. Up to now, no laser ablation study allows us to clearly discriminate between the two scenarios for noble gas origin on Earth because of the scarcity of data and the poor accuracy (Raquin *et al.*, 2008; Colin *et al.*, 2015; Péron *et al.*, 2016).

We analysed by laser ablation the noble gas compositions (He, Ne, Ar) of twenty vesicles of two submarine glass samples from Fernandina volcano (Galápagos), previously imaged via X-ray microtomography to locate the vesicles (Supplementary Information and Table S-1), with the aim of understanding the air contamination mechanisms, and refining the Earth's primordial  $^{20}\text{Ne}/^{22}\text{Ne}$  and  $^{38}\text{Ar}/^{36}\text{Ar}$  ratios to evaluate the two models for noble gas origin on Earth; the solar wind implantation model (Trieloff *et al.*, 2000; Raquin and Moreira, 2009) and the solar nebula gas dissolution model (Yokochi and Marty, 2004; Mukhopadhyay, 2012). These OIB samples, AHA-NEMO2-D22A and AHA-NEMO2-D22B, were chosen due to their very primitive He and Ne compositions (Kurz *et al.*, 2009), relatively high gas concentrations and thick glassy rinds (results are in Tables S-2 and S-3).

1. Institut de Physique du Globe de Paris - Sorbonne Paris Cité, UMR CNRS 7154, Université Paris Diderot, 1 Rue Jussieu, 75005 Paris, France

\* Corresponding author (email: peron@ipgp.fr)

2. Institute of Earth Sciences, University of Lausanne, Géopolis Building, CH-1015 Lausanne, Switzerland

3. Marine Chemistry and Geochemistry, MS #25, Clark 421, Woods Hole Oceanographic Institution, Woods Hole, MA 02543, United States



## Evidence for a Ne-B Component in the Mantle

All the new vesicles analysed show similar isotopic compositions, with only two exceptions (vesicles V4B and V16B; Figs. 1, 2 and Table S-3). Vesicles V4B and V16B may be contaminated by air since their  $^{20}\text{Ne}/^{22}\text{Ne}$  and  $^{40}\text{Ar}/^{36}\text{Ar}$  ratios are lower and tend to atmospheric ratios. Small but subtle cracks are observed just above these bubbles on the X-ray microtomography images (Figs. S-1, S-2, S-3 and S-4) and must have been hit before piercing these vesicles, mixing air with vesicle gases. This is a new evidence of atmospheric contamination mechanisms. These cracks, typically less than 20  $\mu\text{m}$  wide, are difficult to notice. Except those two vesicles, and the vesicles for which the uncertainties are large (V2B, V5B, V6B, V11B and V2A), the  $^{20}\text{Ne}/^{22}\text{Ne}$  ratio is between  $12.17 \pm 0.13$  and  $12.83 \pm 0.09$  ( $1\sigma$ ), the vesicles have a  $^{38}\text{Ar}/^{36}\text{Ar}$  ratio similar to air (0.188) and the  $^{40}\text{Ar}/^{36}\text{Ar}$  ratio is between  $5809 \pm 425$  and  $8206 \pm 695$  (Table S-3 and Fig. S-5).

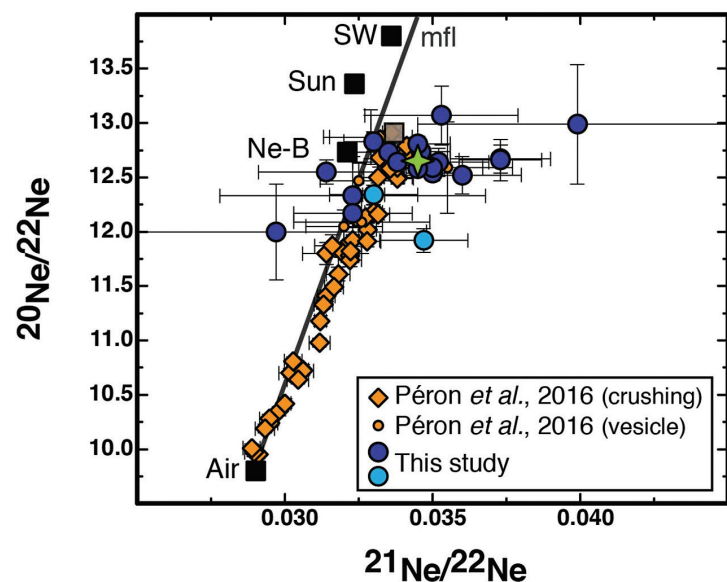


**Figure 1** The three neon isotopes plot for the vesicles. Data from the literature for the same samples (Péron *et al.*, 2016) are in orange diamonds and circles. The new data are in blue circles, the two vesicles in light blue (V4B and V16B) are assumed to be air contaminated (Figs. S-1, S-2). The Fernandina source isotopic composition estimated from the statistical analysis with the new data is indicated with the green star, in comparison with the previous one (Péron *et al.*, 2016) indicated with the grey square. Ne-B (Moreira, 2013), Sun (Heber *et al.*, 2012), solar wind SW (Heber *et al.*, 2009), *mfl* mass fractionation line.

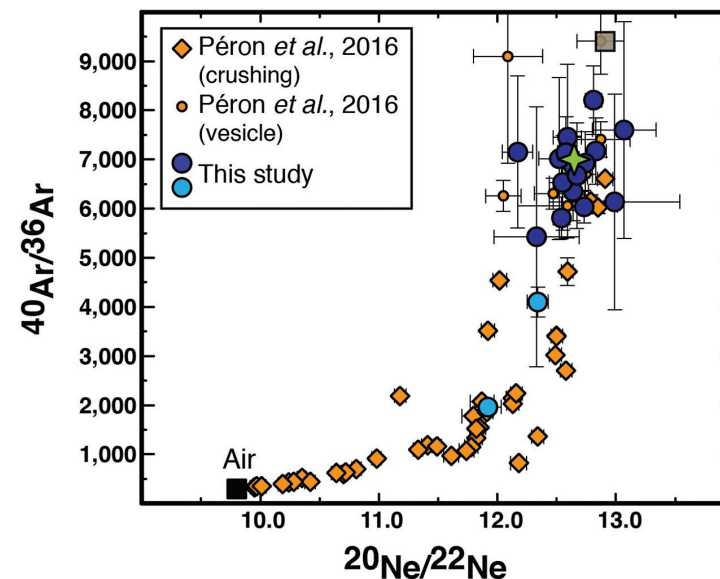


**Figure 2**  $^{40}\text{Ar}/^{36}\text{Ar}$  ratio vs  $^{20}\text{Ne}/^{22}\text{Ne}$  ratio for the vesicles. The latter are in blue circles (vesicles V2A and V11B have too large uncertainties and are not represented). Previous data are in orange diamonds and circles (Péron *et al.*, 2016). The two vesicles in light blue (V4B and V16B) are assumed to be air contaminated, as indicated by the  $^{40}\text{Ar}/^{36}\text{Ar}$  data, along with distribution of microcracks (Figs. S-1, S-2, S-3, S-4, S-8). The Fernandina source isotopic composition inferred from laser ablation data alone is indicated with the green star, in comparison with the previous one (Péron *et al.*, 2016) indicated with the grey square.

The relatively large dataset (20 vesicles) combined with the fact that all the vesicles have similar isotopic compositions (Figs. 1 and 2), suggests that they all sample the same gas. This allows a statistical analysis (Fig. 3) in order to derive precisely the Fernandina source isotopic ratios. In this new approach, a Gaussian distribution is considered for each vesicle isotopic ratio, where the mean is the measured isotopic ratio and sigma is the associated measurement uncertainty, and then the sum of all these Gaussian distributions for a given isotopic ratio gives a cumulative curve. These cumulative curves are thus fitted to obtain overall means (Supplementary Information). This allows us to weight the mean according to measurement uncertainty. We use all the vesicles except the two contaminated ones (V4B and V16B). By fitting the curves with Gaussian distributions on Figure 3 (and Fig. S-6), we obtained a  $^{20}\text{Ne}/^{22}\text{Ne}$  ratio of  $12.65 \pm 0.04$  ( $\sigma/\sqrt{n}$ ), a  $^{21}\text{Ne}/^{22}\text{Ne}$  ratio of  $0.0345 \pm 0.0004$  ( $\sigma/\sqrt{n}$ ) and a  $^{38}\text{Ar}/^{36}\text{Ar}$  ratio of  $0.1887 \pm 0.0006$  ( $\sigma/\sqrt{n}$ ). The  $^{40}\text{Ar}/^{36}\text{Ar}$  distribution could not be fitted with a Gaussian curve but the data show that this ratio is between 6000 and 7000 in the Fernandina source (Fig. S-7).



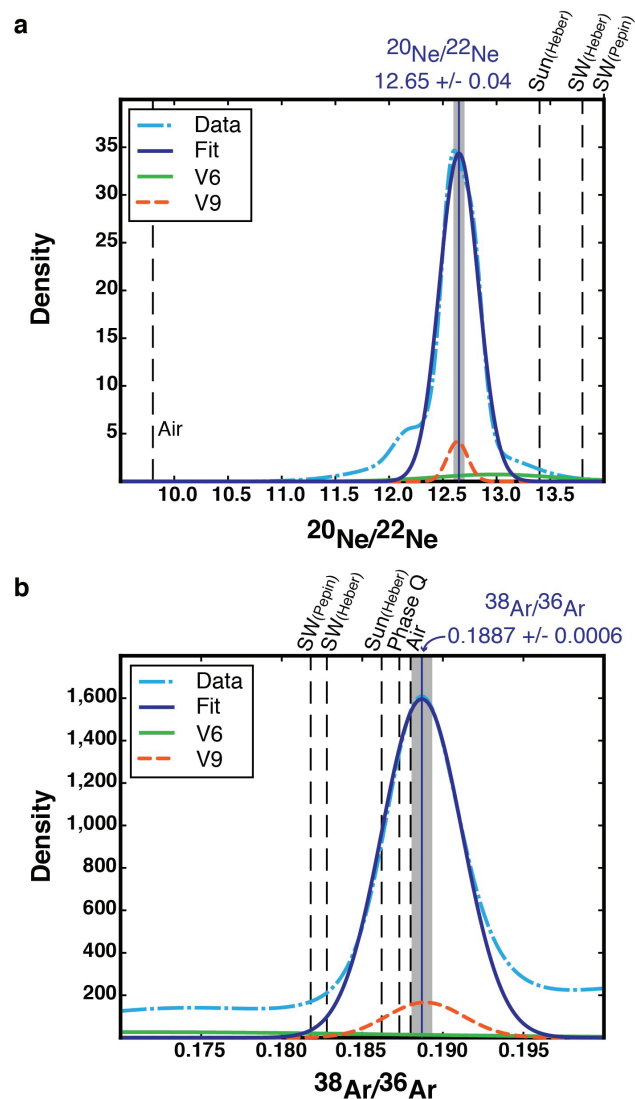


**Figure 3** Gaussian curves obtained (a) for the  $^{20}\text{Ne}/^{22}\text{Ne}$  ratio and (b) for the  $^{38}\text{Ar}/^{36}\text{Ar}$  ratio. The light blue dotted curve is the cumulative curve obtained with the data (except V4B and V16B), the dark blue curve is the Gaussian fit. As an example, the orange dotted curve for vesicle V9 contributes strongly to the cumulative curve, whereas V6 (green curve) is poorly constrained. The mean isotopic ratios, from the statistical analysis, are represented with the blue lines and the corresponding uncertainties ( $\sigma/\sqrt{n}$ ) with the shaded areas. Solar wind (SW) (Heber *et al.*, 2009; Pepin *et al.*, 2012), Sun (Heber *et al.*, 2012), Phase Q (Busemann *et al.*, 2000).

## Discussion and Conclusions

The new results are consistent with previous studies about the Hawaii and Iceland hotspots (Trieloff *et al.*, 2000; Mukhopadhyay, 2012; Colin *et al.*, 2015). The highest values of  $12.91 \pm 0.07$  and  $9407 \pm 672$  for the  $^{20}\text{Ne}/^{22}\text{Ne}$  and  $^{40}\text{Ar}/^{36}\text{Ar}$  ratios respectively obtained in a previous study of the same samples (Péron *et al.*, 2016) seem to be slightly too high for the Fernandina mantle source within  $2\sigma$  uncertainties. Hence, it does not seem appropriate to take the highest values for determining mantle source isotopic ratios. We cannot exclude that isotopic fractionation occurs during bubble formation (Ruzié and Moreira, 2010), which could increase the  $^{20}\text{Ne}/^{22}\text{Ne}$  ratio for a few bubbles, and also that slight sample heterogeneities exist, which could explain the small variability observed between the bubbles. It is thus more suitable to take a mean of the data, provided that the bubbles have similar compositions. The statistical analysis used here provides a new approach for precise determination of isotopic ratios.

As detailed in Supplementary Information, we do not expect contamination of the bubbles. Even if recycling of heavy noble gases (Ar, Kr, Xe) through subduction may occur (Holland and Ballentine, 2006; Kendrick *et al.*, 2011; Parai and Mukhopadhyay, 2015), recycling of He and Ne into the OIB gas-rich source is not significant (Staudacher and Allègre, 1988; Holland and Ballentine, 2006). The  $^{20}\text{Ne}/^{22}\text{Ne}$  ratio of  $12.65 \pm 0.04$  is thus likely to represent the Fernandina source isotopic composition.

The  $^{20}\text{Ne}/^{22}\text{Ne}$  ratio corresponds quite closely to the Ne-B composition. The Ne-B  $^{20}\text{Ne}/^{22}\text{Ne}$  ratio was determined from analyses of gas-rich meteorites and lunar soils, which have been exposed to solar wind irradiation for millions of years (12.52; Black, 1972; 12.8 on average; Eberhardt *et al.*, 1972), and also from numerical simulations (12.73; Raquin and Moreira, 2009; Moreira, 2013; Moreira and Charnoz, 2016). This is the first high precision laser ablation study for Ne, involving enough vesicles for a statistical analysis. The fact that all the vesicles show similar isotopic compositions, in the Ne-B range of values, combined with the lunar soil results, is a strong argument in favour of the solar wind implantation model to explain light noble gas origin on Earth. The new results are consistent with this steady-state (Ne-B) composition and it may not be necessary to invoke non-steady state solar wind implantation onto grains to explain the lower mantle  $^{20}\text{Ne}/^{22}\text{Ne}$  ratio (Péron *et al.*, 2016). Other studies suggest that the  $^{38}\text{Ar}/^{36}\text{Ar}$  ratio is atmospheric in the Earth's mantle (Trieloff *et al.*, 2000; Raquin and Moreira, 2009; Mukhopadhyay, 2012), and lunar soils seem to have a  $^{38}\text{Ar}/^{36}\text{Ar}$  ratio close to the atmospheric value even if the resolution is low (*e.g.*, Eberhardt *et al.*, 1972; Benkert *et al.*, 1993). Hence, the solar wind implantation model could also account for the lower mantle  $^{38}\text{Ar}/^{36}\text{Ar}$  ratio.

Previous step-crushing studies advocated that the early Earth would have captured a primordial atmosphere from solar nebula gas and that noble gases come from the dissolution of this early atmosphere into a magma ocean (Yokochi and Marty, 2004; Mukhopadhyay, 2012). This scenario is problematic for several



reasons. First, the mantle noble gas isotopic composition is different from the solar or solar wind compositions (the Sun  $^{20}\text{Ne}/^{22}\text{Ne}$  ratio would be 13.34; Heber *et al.*, 2012). The solar nebula dissolution model would thus require subduction of atmospheric Ne to lower the  $^{20}\text{Ne}/^{22}\text{Ne}$  ratio from solar to the actual mantle value. However, Ne recycling into the Ne-rich, lower mantle is not significant (Staudacher and Allègre, 1988; Holland and Ballentine, 2006). Finally, this model requires that enough Ne would have been dissolved into the Earth's precursors (Mars-sized objects) because the solar nebula is blown in a few Ma (Wyatt *et al.*, 2003), well before Earth accretion has finished, which may be problematic because those objects cannot capture dense atmospheres.

Implantation of solar wind ions onto grains has also been suggested to explain the very low D/H ratio of the lower mantle (highly negative  $\delta\text{D}$  of  $-218\text{‰}$ ), measured in olivine-hosted melt inclusions of a Baffin Island sample (Hallis *et al.*, 2015). The solar nebula  $\delta\text{D}$  ratio is  $-870\text{‰}$  and so solar wind irradiation, a mechanism able to enrich grains in heavy isotopes, could explain the lower mantle value and could then be one of the sources of water on Earth (Hallis *et al.*, 2015). This scenario offers a simple alternative to explain light volatiles (H, He, Ne) origin on Earth.

This study has put forward two major implications. First, it is more reliable to consider a mean of laser ablation data rather than taking the highest measured values to determine precisely mantle source compositions. Secondly, this new approach supports the model of solar wind irradiation associated with sputtering to explain He and Ne origin on Earth. Solar wind implantation is also likely a major source of Ar and H on Earth.

## Acknowledgements

We thank Lukas Baumgartner for the generous access to the tomography facilities. We also thank Déborah Chavrit, Frédéric Moynier, Alberto E. Saal and John Creech for their constructive comments and discussion on the first versions of this manuscript. We acknowledge the financial support from the UnivEarthS Labex program of Sorbonne Paris Cité (ANR-10-LABX-0023 and ANR-11-IDEX-0005-02). The image for the graphical abstract was designed by Joël Dyon of IPGP.

Editor: Bruce Watson

## Additional Information

**Supplementary Information** accompanies this letter at [www.geochemicalperspectivesletters.org/article1718](http://www.geochemicalperspectivesletters.org/article1718)

**Reprints and permission information** are available online at <http://www.geochemicalperspectivesletters.org/copyright-and-permissions>

**Cite this letter as:** Péron, S., Moreira, M., Putlitz, B., Kurz, M.D. (2017) Solar wind implantation supplied light volatiles during the first stage of Earth accretion. *Geochem. Persp. Let.* 3, 151–159.

## References

- ALLÈGRE, C.J., STAUDACHER, T., SARDA, P., KURZ, M.D. (1983) Constraints on evolution of Earth's mantle from rare gas systematics. *Nature* 303, 762–766.
- BALLENTINE, C., BARFOD, D. (2000) The origin of air-like noble gases in MORB and OIB. *Earth and Planetary Science Letters* 180, 39–48.
- BENKERT, J.-P., BAUR, H., SIGNER, P., WIELER, R. (1993) He, Ne and Ar from the Solar Wind and Solar Energetic Particles in lunar ilmenites and pyroxenes. *Journal of Geophysical Research* 98, 13147–13162.
- BLACK, D.C. (1972) On the origins of trapped helium, neon and argon isotopic variations in meteorites—I. Gas-rich meteorites, lunar soil and breccia. *Geochimica et Cosmochimica Acta* 36, 347–375.
- BURNARD, P. (1999) The bubble-by-bubble volatile evolution of two mid-ocean ridge basalts. *Earth and Planetary Science Letters* 174, 199–211.
- BURNARD, P., GRAHAM, D., TURNER, G. (1997) Vesicle-specific noble gas analyses of “popping rock”: implications for primordial noble gases in the Earth. *Science* 276, 568–571.
- BUSEMANN, H., BAUR, H., WIELER, R. (2000) Primordial noble gases in “phase Q” in carbonaceous and ordinary chondrites studied by closed-system stepped etching. *Meteoritics and Planetary Science* 35, 949–973.
- COLIN, A., MOREIRA, M., GAUTHERON, C., BURNARD, P. (2015) Constraints on the noble gas composition of the deep mantle by bubble-by-bubble analysis of a volcanic glass sample from Iceland. *Chemical Geology* 417, 173–183.
- EBERHARDT, P., GEISS, J., GRAF, H., GRÖGLER, N., MENDIA, M.D., MÖRGELI, M., SCHWALLER, H., STETTLER, A., KRÄHENBÜHL, U., VON GUNTEN, H.R. (1972) Trapped solar wind noble gases in Apollo 12 lunar fines 12001 and Apollo 11 breccia 10046. *Proceedings of the Third Lunar Science Conference, Supplement 3, Geochimica et Cosmochimica Acta, The MIT press* 2, 1821–1856.
- HALLIS, L.J., HUSS, G.R., NAGASHIMA, K., TAYLOR, G.J., HALLDÖRSSON, S.A., HILTON, D.R., MOTT, M.J., MEECH, K.J. (2015) Evidence for primordial water in Earth's deep mantle. *Science* 350, 795–797.
- HEBER, V.S., WIELER, R., BAUR, H., OLINGER, C., FRIEDMANN, A., BURNETT, D.S. (2009) Noble gas composition of the solar wind as collected by the Genesis mission. *Geochimica et Cosmochimica Acta* 73, 7414–7432.
- HEBER, V.S., BAUR, H., BOCHSLER, P., MCKEEGAN, K.D., NEUGEBAUER, M., REISENFELD, D.B., WIELER, R., WIENS, R.C. (2012) Isotopic Mass Fractionation of Solar Wind: Evidence from Fast and Slow Solar Wind Collected by the Genesis mission. *The Astrophysical Journal* 759, 121.
- HOLLAND, G., BALLENTINE, C.J. (2006) Seawater subduction controls the heavy noble gas composition of the mantle. *Nature* 441, 186–191.
- KENDRICK, M.A., SCAMBELLURI, M., HONDA, M., PHILLIPS, D. (2011) High abundances of noble gas and chlorine delivered to the mantle by serpentine subduction. *Nature Geoscience* 4, 807–812.
- KURZ, M.D., CURTICE, J., FORNARI, D., GEIST, D., MOREIRA, M. (2009) Primitive neon from the center of the Galápagos hotspot. *Earth and Planetary Science Letters* 286, 23–34.
- MOREIRA, M. (2013) Noble gas constraints on the origin and evolution of Earth's volatiles. *Geochemical Perspectives* 2, 229–403.



- MOREIRA, M., CHARNOZ, S. (2016) The origin of the neon isotopes in chondrites and on Earth. *Earth and Planetary Science Letters* 433, 249–256.
- MUKHOPADHYAY, S. (2012) Early differentiation and volatile accretion recorded in deep mantle Neon and Xenon. *Nature* 486, 101–104.
- PARAI, R., MUKHOPADHYAY, S. (2015) The evolution of MORB and plume mantle volatile budgets: Constraints from fission Xe isotopes in Southwest Indian Ridge basalts. *Geochemistry, Geophysics, Geosystems* 16, 719–735.
- PEPIN, R.O., SCHLUTTER, D.J., BECKER, R.H., REISENFELD, D.B. (2012) Helium, neon, and argon composition of the solar wind as recorded in gold and other Genesis collector materials. *Geochimica et Cosmochimica Acta* 89, 62–80.
- PÉRON, S., MOREIRA, M., COLIN, A., ARBARET, L., PUTLITZ, B., KURZ, M.D. (2016) Neon isotopic composition of the mantle constrained by single vesicle analyses. *Earth and Planetary Science Letters* 449, 145–154.
- RAQUIN, A., MOREIRA, M. (2009) Atmospheric  $^{38}\text{Ar}/^{36}\text{Ar}$  in the mantle: Implications for the nature of the terrestrial parent bodies. *Earth and Planetary Science Letters* 287, 551–558.
- RAQUIN, A., MOREIRA, M., GUILLON, F. (2008) He, Ne and Ar systematics in single vesicles: Mantle isotopic ratios and origin of the air component in basaltic glasses. *Earth and Planetary Science Letters* 274, 142–150.
- RUZIÉ, L., MOREIRA, M. (2010) Magma degassing process during Plinian eruptions. *Journal of Volcanology and Geothermal Research* 192, 142–150.
- STAUDACHER, T., ALLÈGRE, C.J. (1988) Recycling of oceanic crust and sediments: the noble gas subduction barrier. *Earth and Planetary Science Letters* 89, 173–183.
- TRIELOFF, M., KUNZ, J., CLAGUE, D.A., HARRISON, D., ALLÈGRE, C.J. (2000) The nature of pristine noble gases in mantle plumes. *Science* 288, 1036–1038.
- WYATT, M.C., DENT, W.R.F., GREAVES, J.S. (2003) SCUBA observations of dust around Lindroos stars: evidence for a substantial submillimetre disc population. *Monthly Notices of the Royal Astronomical Society* 342, 876–888.
- YOKOCHI, R., MARTY, B. (2004) A determination of the neon isotopic composition of the deep mantle. *Earth and Planetary Science Letters* 225, 77–88.

## ■ Solar wind implantation supplied light volatiles during the first stage of Earth accretion

S. Péron<sup>1\*</sup>, M. Moreira<sup>1</sup>, B. Putlitz<sup>2</sup>, M.D. Kurz<sup>3</sup>

### ■ Supplementary Information

The Supplementary Information includes:

- Material and Method
- Figures S-1 to S-8
- Tables S-1 to S-5
- Supplementary Information References

### Material and Method

The method we followed, detailed hereafter, is similar to that described in Péron *et al.* (2016).

### Samples

The two studied samples, AHA-NEMO2-D22A and AHA-NEMO2-D22B, were collected during the AHA-NEMO2 cruise on the western flank of Fernandina (Galápagos hotspot) (Geist *et al.*, 2006). We selected big glass chunks (centimetre-sized) for laser ablation analyses and then polished them in order to have two large and flat parallel faces. It is better to have flat faces to focus the laser beam.

1. Institut de Physique du Globe de Paris - Sorbonne Paris Cité, UMR CNRS 7154, Université Paris Diderot, 1 Rue Jussieu, 75005 Paris, France
- \* Corresponding author (email: peron@ipgp.fr)
2. Institute of Earth Sciences, University of Lausanne, Géopolis Building, CH-1015 Lausanne, Switzerland
3. Marine Chemistry and Geochemistry, MS #25, Clark 421, Woods Hole Oceanographic Institution, Woods Hole, MA 02543, United States



## X-ray microtomography acquisitions

X-ray microtomography is of huge importance for laser ablation since the samples have low vesicularities (around 3–4 %; Péron *et al.*, 2016). This non-destructive technique allows to precisely locate the bubbles in 3D before piercing them with the laser and to ensure that the vesicles are intact (*i.e.* that they are not connected to air via cracks).

The X-ray microtomography acquisitions were conducted at the Institute of Earth Sciences (Lausanne, Switzerland) on a Skyscan 1173 Brucker's microtomograph. Sample images are obtained following two steps, (a) image acquisition, and (b) image reconstruction including artefact corrections (Ketcham and Carlson, 2001). For the volumetric reconstruction, a Feldkamp algorithm was used as implemented by the Skyscan Software package. Slices were corrected for beam hardening, misalignment and ring artifacts. Examples of slices are shown in Figures S-1, S-2, S-3 and S-4. We followed the same procedure as detailed in a previous study (Péron *et al.*, 2016). The acquisition parameters as well as the resolution for each sample piece are indicated in Table S-1.

## Laser ablation analyses

After being polished and imaged via X-ray microtomography, the samples were cleaned with ethanol and acetone. In addition, if weathering marks were visible, the samples were cleaned in oxalic acid (1 %) on a hot plate (60–80 °C) and then rinsed with distilled water.

The samples were then loaded into the laser cell, which was baked at 100 °C for several days. It was sometimes necessary to wait for two weeks before the blanks were sufficiently low to start the analyses. Laser ablation analyses were started as soon as the line blanks were about  $2.8 \times 10^{-10}$  cm<sup>3</sup> of <sup>4</sup>He, less than  $1.8 \times 10^{-13}$  cm<sup>3</sup> of <sup>22</sup>Ne and less than  $1.8 \times 10^{-12}$  cm<sup>3</sup> of <sup>36</sup>Ar. To target the bubbles, an excimer (argon fluoride) laser of wavelength 193 nm was used (ATLEX-300i system) and the pressure in the laser cell was recorded with a MKS Baratron® manometer. A huge pressure increase meant that a bubble had been reached. If no vesicle was reached, the laser cell was pumped before starting a new ablation. The majority of the vesicles were reached in one laser shot but for a few bubbles it was necessary to perform several cycles of ablation/pumping. Since the manometer was calibrated with an air standard, we used the pressure increases to calculate the CO<sub>2</sub> quantities in the vesicles, assuming that CO<sub>2</sub> is the major gas (Moore *et al.*, 1977). After piercing a vesicle, gases were purified with a Ti getter (at 800 °C for 5 minutes and then at ambient temperature) and a SAES getter and were then trapped onto activated charcoal (except He). Vesicles between 10 and 220 µm deep were analysed (Table S-2) and no influence of depth on the vesicle compositions has been noticed.

Since gases dissolved into the matrix were also released during the ablation (this could be seen on the manometric signal), we corrected the laser ablation analyses with matrix blanks. For that, we pierced the matrix during the same

ablation time as for reaching the bubbles (Tables S-4 and S-5). We noticed that the matrix of all sample pieces has an atmospheric composition (Table S-5) and that the ablation time does not seem to have an influence on the matrix blank composition. Hence, we corrected the vesicle composition with a matrix blank that was carried out just before or just after the vesicle analysis. The He matrix blank represented less than 7 % for all the bubbles (except vesicle V11 for which the blank was 12 %), the Ne matrix blank was less than 25 % for the majority of the vesicles (otherwise the Ne matrix blank was between 45 % and 65 % for a few bubbles), the Ar matrix blank was between 25 % and 90 %. Noble gases were measured on a Noblesse multi-collector mass spectrometer (Nu instruments ©). To correct for interferences of HF<sup>+</sup> and <sup>40</sup>Ar<sup>++</sup> with <sup>20</sup>Ne<sup>+</sup> and also interferences of CO<sub>2</sub><sup>++</sup> with <sup>22</sup>Ne<sup>+</sup>, we performed a scan of HF before introducing the neon into the mass spectrometer and during the neon cycles we also analysed the mass 40 and 44. Since we determined the ionisation ratios <sup>40</sup>Ar<sup>++</sup>/<sup>40</sup>Ar<sup>+</sup> (0.075) and CO<sub>2</sub><sup>++</sup>/CO<sub>2</sub><sup>+</sup> (0.01) for the Noblesse mass spectrometer, we then corrected the <sup>20</sup>Ne and <sup>22</sup>Ne abundances. Two standards were used in this study, an air standard and a homemade standard, which was previously described (Péron *et al.*, 2016).

The <sup>4</sup>He/<sup>40</sup>Ar\* ratio is a proxy of degassing process because of helium and argon solubility differences and undegassed samples have  $3 < ^4\text{He}/^{40}\text{Ar}^* < 5$  (Moreira and Kurz, 2013). The <sup>4</sup>He/<sup>40</sup>Ar\* ratio of the analysed vesicles is  $3.50 \pm 0.06$  (Table S-3), therefore the samples were not extensively degassed, and noble gases were not fractionated between each other.

Laser ablation analysis, associated with X-ray microtomography, is a powerful technique to measure mantle source compositions without atmospheric contamination. Indeed, all the vesicles have similar compositions (Figs. 1, 2, S-5 and S-8), except the two vesicles V4B and V16B, for which cracks were identified (Figs. S-1 and S-2). Figure S-8 shows that the vesicle <sup>40</sup>Ar/<sup>36</sup>Ar ratios do not change depending on <sup>36</sup>Ar concentrations (except for vesicles V4B and V16B), which is a strong argument against atmospheric contamination of the bubbles through invisible cracks. Matrix effects (Raquin *et al.*, 2008) must be very limited on these new analyses. Indeed, the matrix blank compositions are homogeneous and do not depend on the ablation time (Tables S-4 and S-5). Moreover, the ablation times for reaching the vesicles (Table S-3) were typically very short. For all these reasons, we do not expect post-eruption contamination of the bubbles, either on the seafloor or from the matrix during laser ablation.

Moreover, the Cl/K ratios for samples AHA-NEMO2-D22A and D22B are about 0.04–0.06 (Alberto Saal, personal communication), which corresponds to values for uncontaminated OIBs (Koleszar *et al.*, 2009). This suggests that assimilation of altered oceanic crust has not occurred or at least has been rather limited for these samples.



## Statistical analysis

All the vesicles analysed show similar isotopic compositions (except the vesicles V4B and V16B which are contaminated). This means that they all represent the same source and it is interesting to compute mean isotopic ratios in order to evaluate the source composition. First a Gaussian distribution  $f$  is considered for each vesicle isotopic ratio,

$$f = \frac{1}{\sigma\sqrt{2\pi}} \exp\left(\frac{-(x-\mu)^2}{2\sigma^2}\right)$$

where  $\mu$  is the measured isotopic ratio and  $\sigma$  is the associated measurement uncertainty. The interval  $x$  is chosen depending on the isotopic ratio considered. For example, for the  $^{20}\text{Ne}/^{22}\text{Ne}$  ratio,  $x$  varies from 9 to 14 (Fig. 3). Then, the sum of all the Gaussian distributions for a given isotopic ratio gives a cumulative global curve. This method was used for the  $^{20}\text{Ne}/^{22}\text{Ne}$ ,  $^{21}\text{Ne}/^{22}\text{Ne}$ ,  $^{38}\text{Ar}/^{36}\text{Ar}$  and  $^{40}\text{Ar}/^{36}\text{Ar}$  ratios (Figs. 3, S-6 and S-7). In each case, the global curves also correspond to Gaussian distributions except for the  $^{40}\text{Ar}/^{36}\text{Ar}$  ratio. This shows that mean isotopic ratios have to be taken instead of maximum values. Therefore, these global curves are fitted with Gaussian curves (except for the  $^{40}\text{Ar}/^{36}\text{Ar}$  ratio) to derive mean isotopic ratios and the associated uncertainty  $\sigma$ . For this statistical analysis, all the vesicles except the two contaminated ones (V4B and V16B) are used, which consists of 18 data.

It is important to note that this statistical analysis can be used providing that all the data represent the same composition, which is the case in this study as already mentioned. Moreover, this new approach is particularly useful when a small number of data are considered because it gives more weight to the more accurate data. This is shown on Figures 3 and S-5 where the vesicle V9B associated with low uncertainties has much more influence on the global cumulative curves than vesicle V6B for which uncertainties are large. The final errors on the computed mean isotopic ratios are thus  $\sigma/\sqrt{n}$  (with  $n = 18$ ).

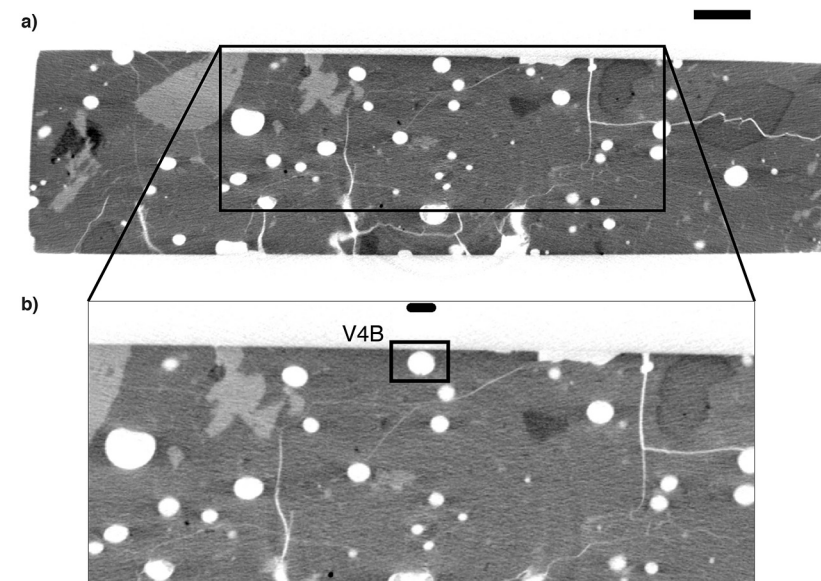


**Figure S-1** X-ray microtomography image of the sample AHA-NEMO2-D22B (piece 1, Table S-1). **(a)** Example of one slice of the sample with the vesicle V4B at the middle top (the scale bar is 1,000  $\mu\text{m}$ ) and **(b)** is a zoom on this vesicle (black square) to show the location (the scale bar is 300  $\mu\text{m}$ ). On these images, vesicles are in white and the glass matrix is in grey as well as a few crystals. A network of cracks (in white) is clearly visible. Vesicle V4B is very close to the surface and is likely contaminated due to a small connection to air.



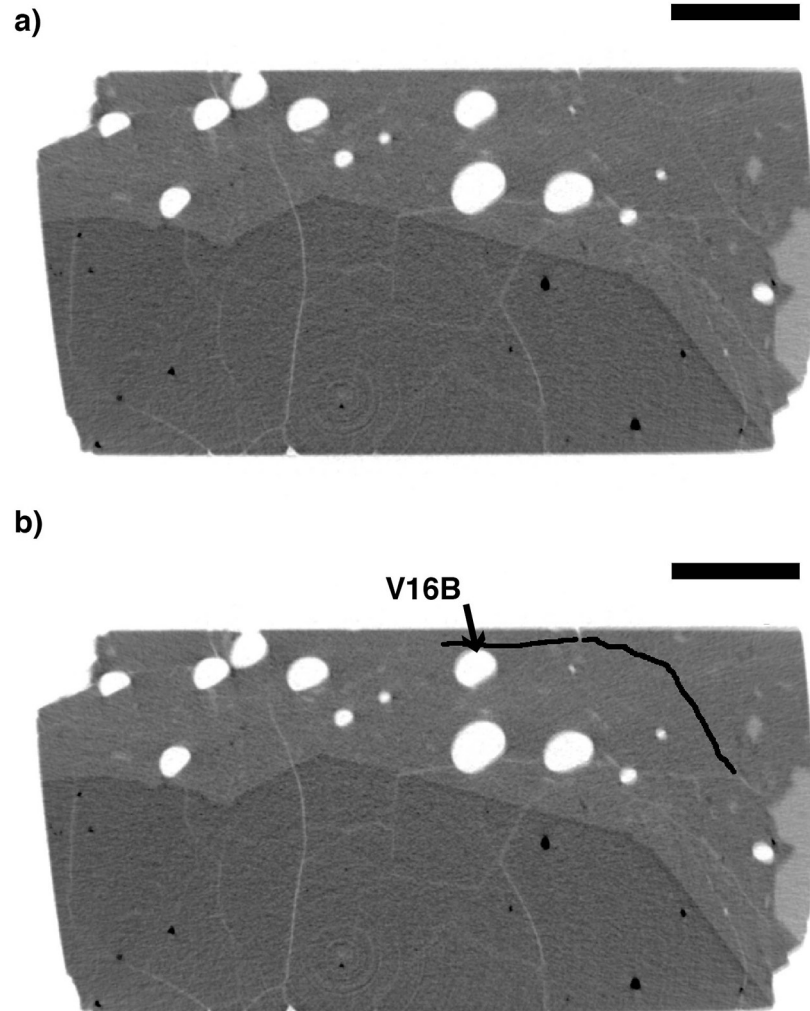


**Figure S-2** X-ray microtomography image of the sample AHA-NEMO2-D22B (piece 2, Table S-1) to show the location of vesicle V16B. The original slice is represented in (a) and the very tiny crack just above the vesicle V16B is indicated by a black line in (b). To reach the vesicle, the laser also pierced the crack, which introduced air. The scale bars are 1,000  $\mu\text{m}$ . (Refer also to the legend of Fig. S-1).

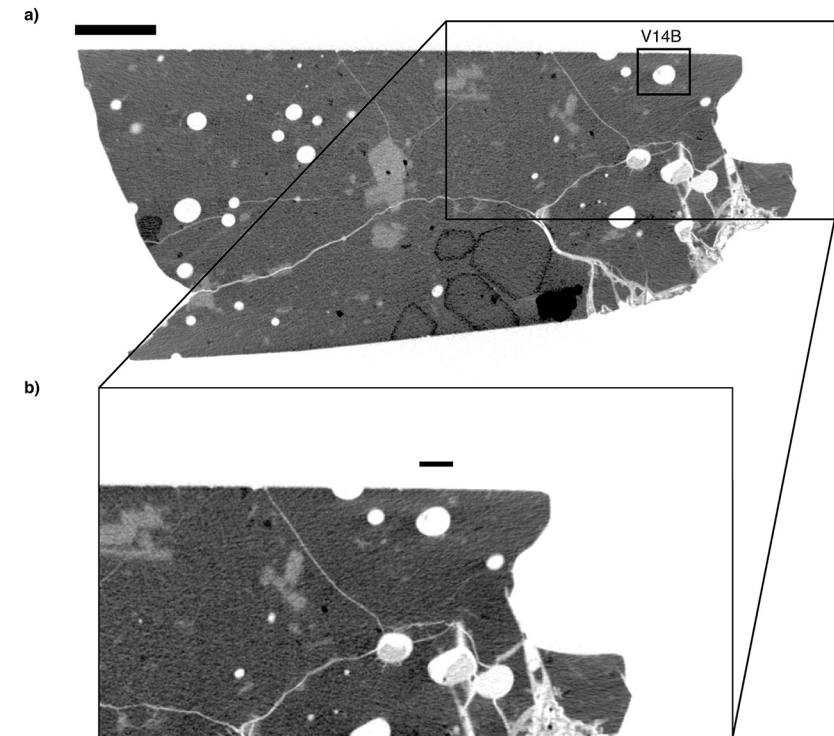


**Figure S-3** X-ray microtomography image of the sample AHA-NEMO2-D22B (piece 3, Table S-1) to show the location of vesicle V14B. The original slice is represented in (a) and vesicle V14B is indicated with a black square (the scale bar is 1,000  $\mu\text{m}$ ), (b) is a zoom on this vesicle to show what surrounds it (the scale bar is 260  $\mu\text{m}$ ). (Refer also to the legend of Fig. S-1). Vesicle V14B has a low  $^{20}\text{Ne}/^{22}\text{Ne}$  ratio (Table S-3) but no crack is visible on the images. This vesicle is unlikely to be contaminated because the  $^{40}\text{Ar}/^{36}\text{Ar}$  ratio is  $7155 \pm 1546$ .



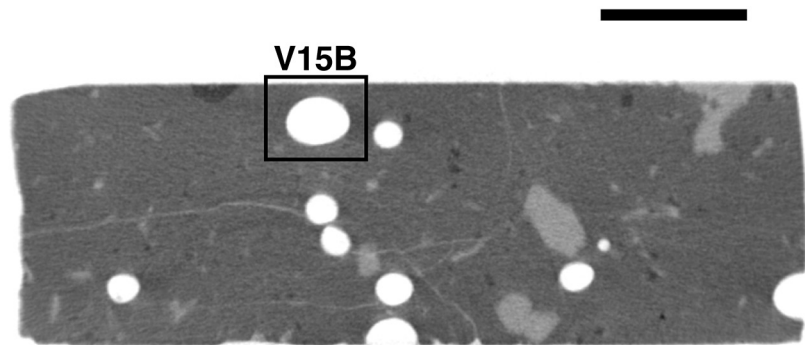


**Figure S-4** X-ray microtomography image of the sample AHA-NEMO2-D22B (piece 2, Table S-1). This shows an example of a non-contaminated vesicle, vesicle V15B, which is the biggest vesicle analysed. The scale bar is 1,000  $\mu\text{m}$ . (Refer also to the legend of Fig. S-1).

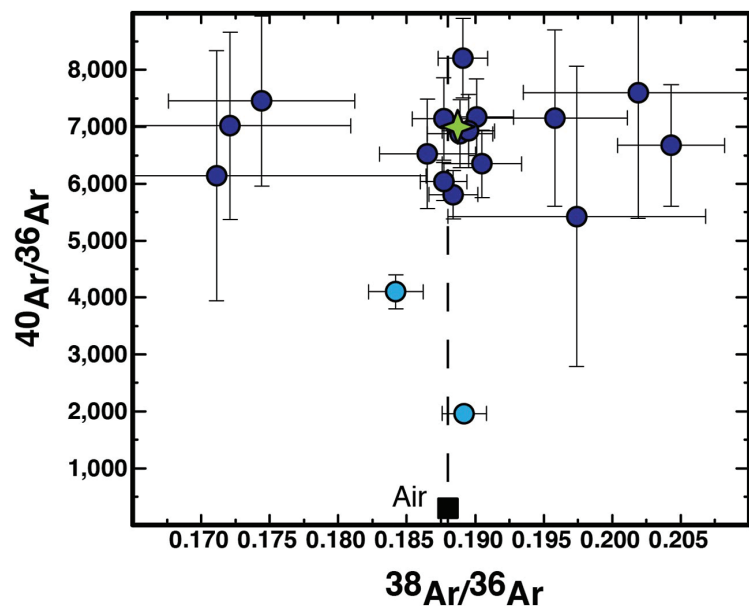


**Figure S-5**  $^{40}\text{Ar}/^{36}\text{Ar}$  vs  $^{38}\text{Ar}/^{36}\text{Ar}$  for the vesicles. The Fernandina (Galápagos) source composition is indicated with the green star. The two light blue circles correspond to the two contaminated vesicles (V4B and V16B). Vesicles V2A and V11B are not represented because their uncertainties are too large.

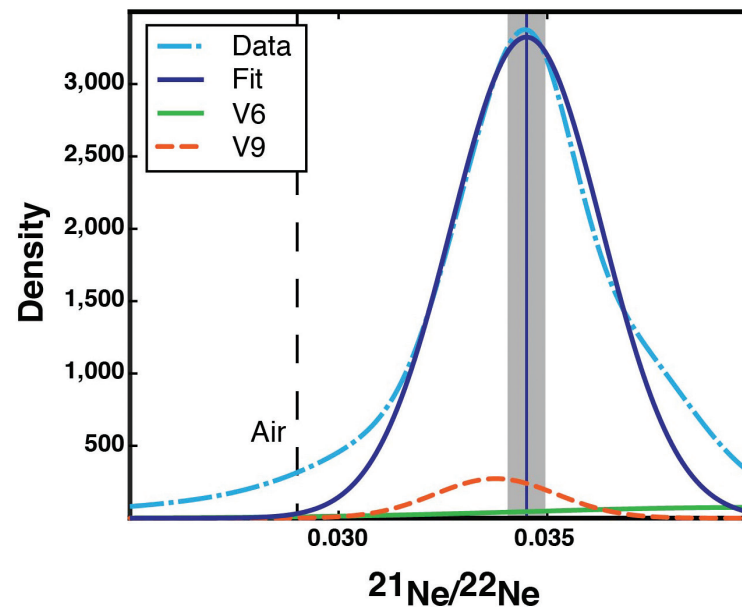


**Figure S-6** Gaussian curves obtained for the  $^{21}\text{Ne}/^{22}\text{Ne}$  ratio. The light blue dotted curve is the cumulative Gaussian curve taking into account all the vesicles (except V4B and V16B), the dark blue curve is the Gaussian fit. Examples of two Gaussian curves are indicated for some vesicles: vesicle V9 (orange dotted curve) has low uncertainties and contributes strongly to the global Gaussian curve, vesicle V6 (green curve) is poorly constrained and has nearly no influence on the global curve. The mean isotopic ratio (0.0345) determined with the statistical analysis is represented with the solid blue line. The shaded area corresponds to  $\sigma/\sqrt{n} = \pm 0.0004$ . For comparison, air composition is indicated.



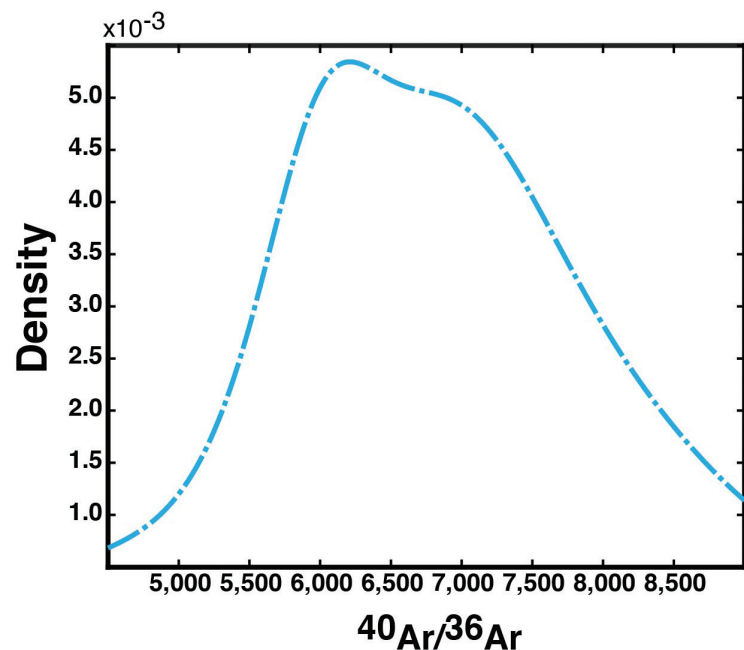


**Figure S-7** Cumulative curve obtained for the  $^{40}\text{Ar}/^{36}\text{Ar}$  ratio taking into account all the vesicles (except V4B and V16B). This curve cannot be correctly fitted with a Gaussian curve. The  $^{40}\text{Ar}/^{36}\text{Ar}$  ratio is between 6000 and 7000 for the Fernandina source.

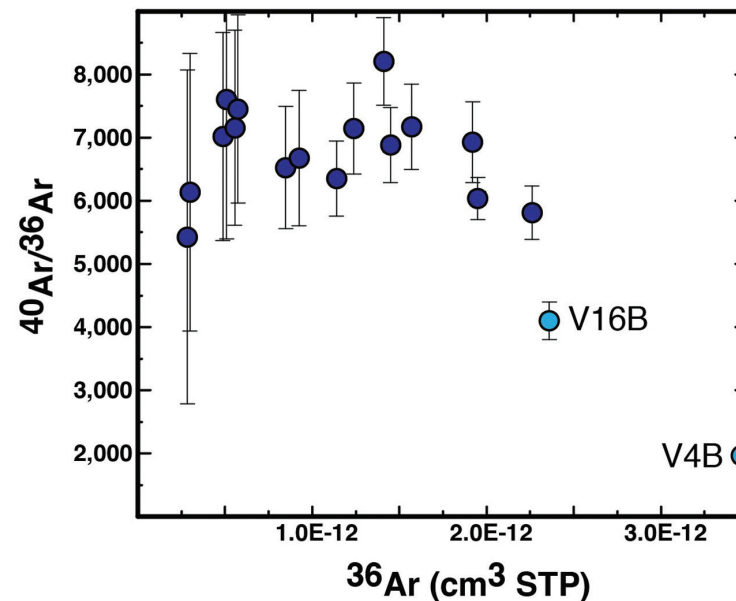


**Figure S-8**  $^{40}\text{Ar}/^{36}\text{Ar}$  vs  $^{36}\text{Ar}$  (in  $\text{cm}^3$  STP) for the vesicles. The two contaminated vesicles (V4B and V16B) are in light blue. Except for these two bubbles, the  $^{40}\text{Ar}/^{36}\text{Ar}$  ratio does not change with the  $^{36}\text{Ar}$  concentration, which indicates that the vesicles are not contaminated by air. Vesicles V2A and V11B are not represented because they have too large uncertainties.

**Table S-1** Acquisition parameters for X-ray microtomography. The experiments were conducted at the Institute of Earth Sciences (Lausanne, Switzerland) on a Skyscan 1173 system. One piece of sample AHA-NEMO2-D22A has been studied and four for sample AHA-NEMO2-D22B. The piece number is indicated as well as the voltage (in kV), the current (in  $\mu\text{A}$ ), the rotation step size (in degrees), the number of frames (which is the number of images taken for one position), the filter type used and the resolution (in  $\mu\text{m}$  per pixel). The resolution in  $\mu\text{m}^3$  per voxel (1 voxel =  $1 \times 1 \times 1$  pixel) is the cubic resolution in  $\mu\text{m}$  per pixel.

Sample	#	Voltage kV	Current $\mu\text{A}$	Rotation step size $^\circ$	Number of frames	Filter	Pixel size $\mu\text{m}$
AHA-NEMO2-D22A	1	70	114	0.225	4	Al 1.0 mm	5.7
AHA-NEMO2-D22B	1	70	114	0.225	4	Al 1.0 mm	8.2
AHA-NEMO2-D22B	2	70	114	0.225	4	Al 1.0 mm	6.4
AHA-NEMO2-D22B	3	70	114	0.225	4	Al 1.0 mm	5.7
AHA-NEMO2-D22B	4	70	114	0.225	8	Al 1.0 mm	9.3



**Table S-2** CO<sub>2</sub> and noble gas (<sup>4</sup>He, <sup>22</sup>Ne and <sup>36</sup>Ar) abundances (in cm<sup>3</sup> STP) for all the vesicles for samples AHA-NEMO2-D22A and AHA-NEMO2-D22B (Fernandina, Galápagos). The ablation time for each vesicle is indicated in brackets. The piece number (refer to Table S-1) and the depth of each vesicle below the sample surface are mentioned. The vesicle volumes were calculated with the 3D Object Counter plugin of ImageJ. The CO<sub>2</sub> contents were determined using the pressure jump recorded on the manometer, calibrated with the air standard, and assuming that CO<sub>2</sub> is the major gas (Moore et al., 1977). Errors are 1 sigma uncertainties.

Sample	#	Depth μm	Volume x10 <sup>6</sup> μm <sup>3</sup>	CO <sub>2</sub> x10 <sup>-4</sup> cm <sup>3</sup>	s	<sup>4</sup> He x10 <sup>-8</sup> cm <sup>3</sup>	s	<sup>22</sup> Ne x10 <sup>-13</sup> cm <sup>3</sup>	s	<sup>36</sup> Ar x10 <sup>-13</sup> cm <sup>3</sup>	s
AHA-NEMO2-D22A vesicles											
V1A (2'02")	1	100	15.6	10.3	1.0	2.06	0.09	3.74	0.29	9.25	0.38
V2A (25")	1	48	11.6	7.45	0.72	1.48	0.09	2.70	0.27	1.72	0.38
AHA-NEMO2-D22B vesicles											
V1B (41")	1	15	34.3	22.1	2.1	4.34	0.08	8.35	0.26	22.6	0.38
V2B (16")	1	20	10.5	6.48	0.64	1.29	0.08	1.90	0.26	5.09	0.36
V3B (2'02")	1	110	29.6	18.9	1.8	3.75	0.08	6.10	0.26	15.7	0.37
V4B (12")	1	22	16.3	10.2	1.0	1.96	0.08	4.51	0.26	34.6	0.42
V5B (30")	1	60	4.1	2.64	0.31	0.51	0.08	0.99	0.26	2.84	0.36
V6B (1'50")	2	50	4.8	3.04	0.34	0.60	0.09	1.01	0.26	3.00	0.37
V7B (16")	4	90	32.5	19.6	1.9	3.82	0.09	6.95	0.33	19.5	0.45
V8B (17")	4	110	19.1	12.6	1.2	2.44	0.09	3.91	0.28	11.4	0.40
V9B (50")	3	155	26.7	16.9	1.6	3.36	0.09	6.40	0.32	14.5	0.42
V10B (40")	3	195	14.8	9.48	0.91	1.89	0.09	3.44	0.28	8.49	0.39
V11B (8")	4	18	1.0	1.41	0.22	0.29	0.09	0.50	0.26	1.08	0.37
V12B (15")	4	100	9.4	5.97	0.59	1.18	0.09	2.67	0.27	4.88	0.38
V13B (23")	3	130	11.5	7.31	0.71	1.45	0.09	2.72	0.27	5.74	0.38
V14B (25")	3	155	11.4	6.87	0.67	1.32	0.09	2.48	0.27	5.57	0.38
V15B (25")	2	90	35.9	22.7	2.1	4.44	0.09	7.38	0.34	19.2	0.41
V16B (3'39")	2	145	25.7	15.8	1.5	3.13	0.09	6.49	0.33	23.6	0.42
V17B (3')	1	220	26.0	15.4	1.5	3.03	0.09	5.59	0.33	12.4	0.39
V18B (45")	2	100	31.2	19.5	1.8	3.86	0.09	6.61	0.36	14.1	0.39



**Table S-3** Isotopic compositions of the vesicles for samples AHA-NEMO2-D22A and AHA-NEMO2-D22B (Fernandina, Galápagos). Ra is the air  $^3\text{He}/^4\text{He}$  ratio and is equal to  $1.384 \times 10^{-6}$  (Clarke *et al.*, 1976).  $^{40}\text{Ar}^*$  is radiogenic  $^{40}\text{Ar}$ . We consider a  $^{40}\text{Ar}/^{36}\text{Ar}$  ratio of 298.6 for the air (Lee *et al.*, 2006) to determine the  $^{40}\text{Ar}/^{36}\text{Ar}$  and  $^4\text{He}/^{40}\text{Ar}^*$  ratios. n.d. means not determined when gases from the vesicle are indistinguishable from the matrix blank. Errors are 1 sigma uncertainties.

Sample	$\text{CO}_2/{}^3\text{He}$ $\times 10^9$	s	${}^3\text{He}/{}^4\text{He}$ (xRa)	s	${}^{20}\text{Ne}/{}^{22}\text{Ne}$	s	${}^{21}\text{Ne}/{}^{22}\text{Ne}$	s	${}^{38}\text{Ar}/{}^{36}\text{Ar}$	s	${}^{40}\text{Ar}/{}^{36}\text{Ar}$	s	${}^4\text{He}/{}^{40}\text{Ar}^*$	s
AHA-NEMO2-D22A vesicles														
V1A	1.55	0.17	23.50	0.56	12.67	0.13	0.0373	0.0017	0.2043	0.0039	6674	1072	3.49	0.62
V2A	1.64	0.19	22.15	0.63	12.66	0.19	0.0373	0.0014	0.1967	0.0145	n.d.	n.d.	3.53	2.52
AHA-NEMO2-D22B vesicles														
V1B	1.62	0.16	22.74	0.49	12.54	0.07	0.0350	0.0009	0.1884	0.0018	5809	425	3.48	0.28
V2B	1.61	0.19	22.60	0.56	13.07	0.27	0.0353	0.0026	0.2019	0.0084	7601	2208	3.47	1.10
V3B	1.56	0.16	23.28	0.52	12.83	0.09	0.0330	0.0010	0.1901	0.0027	7171	674	3.47	0.36
V4B	1.66	0.18	22.61	0.62	11.92	0.11	0.0347	0.0015	0.1892	0.0016	1962	59	3.41	0.19
V5B	1.63	0.34	22.97	0.76	12.33	0.36	0.0323	0.0045	0.1974	0.0094	5426	2641	3.50	1.95
V6B	1.69	0.31	21.58	0.46	12.99	0.55	0.0399	0.0054	0.1711	0.0153	6138	2197	3.43	1.44
V7B	1.62	0.16	22.92	0.43	12.73	0.09	0.0335	0.0011	0.1877	0.0017	6038	332	3.42	0.23
V8B	1.62	0.17	23.16	0.47	12.64	0.13	0.0352	0.0017	0.1905	0.0029	6350	593	3.52	0.39
V9B	1.58	0.16	23.07	0.46	12.64	0.10	0.0338	0.0015	0.1889	0.0024	6880	597	3.51	0.35
V10B	1.53	0.17	23.65	0.58	12.55	0.11	0.0314	0.0023	0.1865	0.0035	6525	966	3.57	0.60
V11B	1.64	0.56	21.79	1.24	12.00	0.44	0.0297	0.0051	n.d.	n.d.	n.d.	n.d.	n.d.	n.d.
V12B	1.54	0.19	23.59	0.54	12.52	0.17	0.0360	0.0020	0.1721	0.0088	7019	1646	3.61	0.96
V13B	1.61	0.19	22.57	0.66	12.59	0.12	0.0350	0.0017	0.1744	0.0068	7453	1490	3.53	0.80
V14B	1.68	0.20	22.46	0.58	12.17	0.13	0.0323	0.0020	0.1958	0.0053	7155	1546	3.45	0.84
V15B	1.60	0.16	23.11	0.45	12.74	0.09	0.0346	0.0010	0.1895	0.0019	6927	642	3.48	0.35
V16B	1.57	0.16	23.36	0.46	12.34	0.09	0.0330	0.0015	0.1842	0.0020	4101	300	3.49	0.30
V17B	1.64	0.17	22.47	0.51	12.58	0.07	0.0345	0.0009	0.1877	0.0023	7142	723	3.56	0.41
V18B	1.59	0.16	22.85	0.56	12.81	0.07	0.0345	0.0011	0.1891	0.0018	8206	695	3.47	0.33



**Table S-4** Noble gas abundances of the matrix blanks (in cm<sup>3</sup> STP) for samples AHA-NEMO2-D22A and AHA-NEMO2-D22B (Fernandina, Galápagos). The ablation times are indicated in brackets. Errors are 1 sigma uncertainties.

Sample	<sup>4</sup> He x10 <sup>-10</sup> cm <sup>3</sup>	s	<sup>22</sup> Ne x10 <sup>-13</sup> cm <sup>3</sup>	s	<sup>36</sup> Ar x10 <sup>-12</sup> cm <sup>3</sup>	s
AHA-NEMO2-D22A matrix						
Blank 1 (2'02")	3.98	0.28	1.01	0.23	1.55	0.03
Blank 2 (25")	3.59	0.28	0.91	0.23	1.17	0.03
AHA-NEMO2-D22B matrix						
Blank 1 (41")	3.69	0.28	1.29	0.23	1.74	0.03
Blank 2 (16")	3.83	0.28	1.50	0.23	1.54	0.03
Blank 3 (2'01")	3.78	0.28	1.15	0.23	1.18	0.03
Blank 4 (15")	3.83	0.28	1.07	0.23	1.46	0.03
Blank 5 (2')	3.69	0.28	1.33	0.23	1.13	0.03
Blank 6 (4'30")	3.90	0.28	0.76	0.23	1.12	0.03
Blank 7 (50")	3.92	0.28	0.79	0.23	1.32	0.03
Blank 8 (16")	4.00	0.28	0.84	0.23	1.20	0.03
Blank 9 (25")	4.37	0.28	0.79	0.23	1.25	0.03
Blank 10 (27")	3.71	0.28	0.91	0.23	1.86	0.03
Blank 11 (3')	3.56	0.28	1.75	0.24	1.98	0.03
Blank 12 (3')	3.85	0.28	0.63	0.23	1.31	0.03
Blank 13 (45")	3.86	0.28	0.74	0.23	1.24	0.03

**Table S-5** Isotopic compositions of the matrix blanks for samples AHA-NEMO2-D22A and AHA-NEMO2-D22B (Fernandina, Galápagos). Errors are 1 sigma uncertainties.

Sample	<sup>3</sup> He/ <sup>4</sup> He (xRa)	s	<sup>20</sup> Ne/ <sup>22</sup> Ne	s	<sup>21</sup> Ne/ <sup>22</sup> Ne	s	<sup>38</sup> Ar/ <sup>36</sup> Ar	s	<sup>40</sup> Ar/ <sup>36</sup> Ar	s
AHA-NEMO2-D22A matrix										
Blank 1 (2'02")	1.9	0.6	10.40	0.16	0.0278	0.0022	0.1901	0.0011	297	2
Blank 2 (25")	1.8	0.6	10.13	0.17	0.0297	0.0024	0.1933	0.0014	296	2
AHA-NEMO2-D22B matrix										
Blank 1 (41")	1.5	0.5	10.26	0.09	0.0247	0.0021	0.1886	0.0016	299	2
Blank 2 (16")	1.0	0.5	10.00	0.09	0.0322	0.0020	0.1839	0.0020	296	3
Blank 3 (2'01")	1.1	0.7	10.18	0.18	0.0285	0.0033	0.1954	0.0018	296	3

**Table S-5** Cont.

Sample	<sup>3</sup> He/ <sup>4</sup> He (xRa)	s	<sup>20</sup> Ne/ <sup>22</sup> Ne	s	<sup>21</sup> Ne/ <sup>22</sup> Ne	s	<sup>38</sup> Ar/ <sup>36</sup> Ar	s	<sup>40</sup> Ar/ <sup>36</sup> Ar	s
Blank 4 (15")	6.5	0.8	10.07	0.16	0.0312	0.0018	0.1913	0.0014	291	3
Blank 5 (2')	1.8	0.4	10.23	0.22	0.0293	0.0019	0.2027	0.0014	309	2
Blank 6 (4'30")	2.2	0.8	9.99	0.17	0.0304	0.0026	0.2001	0.0018	301	2
Blank 7 (50")	15.5	15.0	10.42	0.11	0.0350	0.0027	0.1964	0.0015	290	2
Blank 8 (16")	2.3	5.2	10.26	0.11	0.0305	0.0014	0.2000	0.0014	303	2
Blank 9 (25")	1.1	0.7	10.24	0.15	0.0301	0.0038	0.1889	0.0017	293	2
Blank 10 (27")	2.6	0.6	10.46	0.12	0.0304	0.0028	0.1922	0.0011	300	1
Blank 11 (3')	2.6	0.9	10.02	0.16	0.0308	0.0021	0.2039	0.0013	312	2
Blank 12 (3')	1.0	0.6	10.26	0.21	0.0351	0.0021	0.1989	0.0011	303	2
Blank 13 (45")	1.8	0.6	10.56	0.20	0.0299	0.0020	0.1912	0.0010	301	2

### Supplementary Information References

- CLARKE, W.B., JENKINS, W.J., TOP, Z. (1976) Determination of tritium by mass spectrometric measurement of <sup>3</sup>He. *The International Journal of Applied Radiation and Isotopes* 27, 512–522.
- GEIST, D., FORNARI, D., KURZ, M.D., HARPP, K.S., SOULE, S.A., PERFIT, M.R., KOLESZAR, A.M. (2006) Submarine Fernandina: Magmatism at the leading edge of the Galapagos hot spot. *Geochemistry, Geophysics, Geosystems* 7, Q12007.
- KETCHAM, R.A., CARLSON, W.D. (2001) Acquisition, optimization and interpretation of X-ray computed tomographic imagery: applications to the geosciences. *Computers & Geosciences* 27, 381–400.
- KOLESZAR, A.M., SAAL, A.E., HAURI, E.H., NAGLE, A.N., LIANG, Y., KURZ, M.D. (2009) The volatile contents of the Galapagos plume; evidence for H<sub>2</sub>O and F open system behavior in melt inclusions. *Earth and Planetary Science Letters* 287, 442–452.
- LEE, J.-Y., MARTI, K., SEVERINGHAUS, J.P., KAWAMURA, K., YOO, H.-S., LEE, J., KIM, J. (2006) A redetermination of the isotopic abundances of atmospheric Ar. *Geochimica et Cosmochimica Acta* 70, 4507–4512.
- MOORE, J.G., BATCHELDER, J.N., CUNNINGHAM, C.G. (1977) CO<sub>2</sub>-filled vesicles in mid-ocean basalt. *Journal of Volcanology and Geothermal Research* 2, 309–327.
- MOREIRA, M.A., KURZ, M.D. (2013) Noble Gases as Tracers of Mantle Processes and Magmatic Degassing. In: Burnard, P. (Ed.) *The Noble Gases as Geochemical Tracers*. Springer, Berlin, Heidelberg, 371–391.
- PÉRON, S., MOREIRA, M., COLIN, A., ARBARET, L., PUTLITZ, B., KURZ, M.D. (2016) Neon isotopic composition of the mantle constrained by single vesicle analyses. *Earth and Planetary Science Letters* 449, 145–154.
- RAQUIN, A., MOREIRA, M., GUILLON, F. (2008) He, Ne and Ar systematics in single vesicles: Mantle isotopic ratios and origin of the air component in basaltic glasses. *Earth and Planetary Science Letters* 274, 142–150.

